Antarctic NAT PSC belt of June 2003: Observational validation of the mountain wave seeding hypothesis

S. D. Eckermann,[1] L. Hoffmann,[2] M. Höpfner,[3] D. L. Wu,[4] and M. J. Alexander[5]

Received 10 November 2008; accepted 12 December 2008; published 22 January 2009.

[1] Satellite observations of polar stratospheric clouds (PSCs) over Antarctica in June 2003 revealed small nitric acid trihydrate (NAT) particles forming suddenly along the vortex edge. Models suggest the trigger was mountain waves over the Antarctic Peninsula (AP) forming ice for NAT nucleation. We test this hypothesis by analyzing perturbations in stratospheric radiances from the Atmospheric Infrared Sounder (AIRS). AIRS data show mountain waves over the AP on 10–14 June, with no resolved wave activity before or after. Peak wave temperature amplitudes derived from independent 40 hPa channels all return values of 10–12 K, in agreement with values used to model this NAT event. These observations support a NAT wake from a small region of mountain wave activity over the AP as the source of this circumpolar NAT outbreak. **Citation:** Eckermann, S. D., L. Hoffmann, M. Höpfner, D. L. Wu, and M. J. Alexander (2009), Antarctic NAT PSC belt of June 2003: Observational validation of the mountain wave seeding hypothesis, *Geophys. Res. Lett.*, *36*, L02807, doi:10.1029/2008GL036629.

1. Introduction

[2] Each winter, PSCs form as polar stratospheric temperatures drop below ~195 K. Three nominal PSC types – nitric acid trihydrate (NAT), supercooled ternary solutions (STS) and ice – can exist at progressively lower temperatures T ($T_{ice} < T_{STS} < T_{NAT}$). The cold interior of the Antarctic polar vortex supports a persistent polar cap of PSCs that converts reservoir chlorine species into activated forms that destroy ozone. A stable meridional temperature gradient drives strong vortex-edge winds that limit lateral mixing.

[3] This temperature gradient can cause PSC types to vary with equivalent latitude. Near the vortex edge where $T_{STS} < T < T_{NAT}$, a circumpolar "freezing belt" of NAT PSCs can exist [*Tabazadeh et al.*, 2001]. If NAT particles form then remain within freezing-belt latitudes for several or more days, they can grow to sizes large enough to sediment to lower sublimation altitudes. Over time this process can denitrify the stratosphere, accentuating springtime ozone loss by removing odd nitrogen compounds that sequester activated chlorine. How, when or if NAT forms in these regions depends on dominant nucleation mechanisms, which remain uncertain and controversial [*Lowe and MacKenzie*, 2008].

2. June 2003 NAT PSC Outbreak

[4] The Michelson Interferometer for Passive Atmospheric Sounding (MIPAS) performed high spectral resolution limb measurements of the Antarctic winter stratosphere in 2003. A color-ratio algorithm described by *Höpfner et al.* [2006a] enabled PSCs of different types to be discriminated.

[5] Figure 1, adapted from *Höpfner et al.* [2006b], maps all PSCs measured by MIPAS on 6 selected days in June 2003. Red squares show solid NAT PSCs of ≤ 3 μm radius. A NAT freezing belt could exist throughout early June (orange band), yet no NAT PSCs were observed. This suddenly changed on 10–11 June when small NAT particles streamed from a genesis region near the Antarctic Peninsula (AP) (Figure 1d), a feature observed more strongly on 12 June and leading 3–4 days later to a freezing belt of solid NAT particles most of the way around Antarctica (Figure 1f).

[6] *Höpfner et al.* [2006b] modeled this event using a stratospheric trajectory model with microphysics under various proposed NAT nucleation mechanisms. No simulation reproduced these observations until mountain wave-induced temperature perturbations were considered. A mountain wave forecasting algorithm [*Eckermann et al.*, 2006a] predicted stratospheric temperature perturbations of ~±10 K over the AP on 10–14 June with little or no wave activity before and after. By inserting these perturbations into their model, the observations were well reproduced via NAT nucleating heterogeneously on ice formed in the cooling phases of AP mountain waves. The simulation reproduced the sudden onset of NAT on 11 June near the AP. The persistence of wave activity through 14–15 June provided a constant source of ice on which NAT could nucleate, and a continuous wake of solid NAT that swept out a circumpolar NAT freezing belt by 15 June.

[7] This explanation relies on model predictions of 10–15 K stratospheric mountain wave amplitudes over the AP during this event. Observational validation of these mountain wave predictions remains the key missing test of this hypothesis.

3. Mountain Waves in AIRS Radiances

[8] AIRS scans cross-track in 90 step-and-stare measurements distributed symmetrically either side of nadir. Horizontal measurement footprints are ~13 × 13 km^2 at nadir and ~31 × 21 km^2 at the far off-nadir views, with a total cross-track swath of ~1650 km. As scans repeat, "pushbroom" radiance images are swept out. Despite having deep vertical weighting functions, the high horizontal resolution

[1]Space Science Division, Naval Research Laboratory, Washington, D. C., USA.
[2]Forschungszentrum Jülich, Jülich, Germany.
[3]Forschungszentrum Karlsruhe, Karlsruhe, Germany.
[4]Jet Propulsion Laboratory, California Institute of Technology, Pasadena, California, USA.
[5]Northwest Research Associates, Boulder, Colorado, USA.

0094-8276/09/2008GL036629

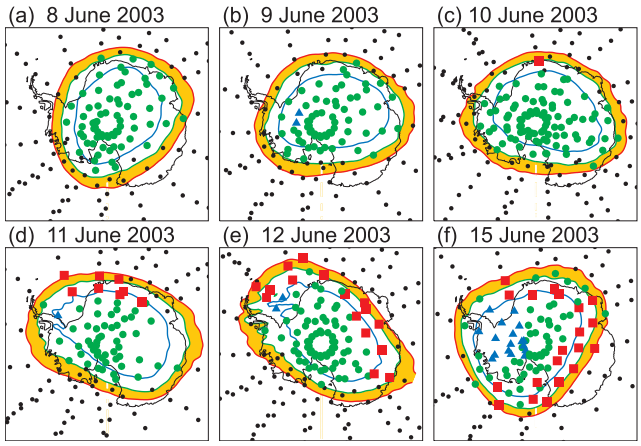

Figure 1. MIPAS Antarctic PSC measurements on indicated dates (adapted from *Höpfner et al.* [2006b]) at ~21 km altitude. Red squares show NAT particles with radii <3 μm, blue triangles show ice, green circles show other PSC types (either STS, large NAT or thin ice). Red, green and blue curves mark NAT, STS and ice equilibrium formation thresholds, respectively, based on analysis temperatures. Orange band marks the region $T_{STS} < T < T_{NAT}$.

and radiometric precision of these measurements allow short deep gravity waves to be resolved, particularly in stratospheric channels negligibly impacted by tropospheric moisture [*Alexander and Barnet*, 2007; *Alexander and Teitelbaum*, 2007; *Eckermann et al.*, 2007].

[9] Since AIRS has over 2300 channels, to both thin the data and reduce noise we averaged Level 1b radiances from a subset of thermal channels with similar vertical weighting functions. We focus initially on an 80 hPa product derived by averaging radiances from channels 92, 98, 104, 105, 110, 111, 116, 117, 122, 123, 128, 129, 134, and 140. Radiances with horizontal scales $\gtrsim$600 km were fitted as in *Eckermann et al.* [2006b] then subtracted from the data to leave small-scale residuals. We applied 3 × 3 point smoothing to reduce noise further and accentuate any geophysical wave signals.

[10] Figure 2 plots a time sequence of 80 hPa radiance residuals over the AP for overpasses from 8–15 June 2003. On 8–9 June 2003 there is no resolved wave structure. Late on 10 June we see first evidence of weak wave oscillations in Figure 2d. Oscillations intensify and spread on 11 June (panels e–f), peak in amplitude on 12–13 June (panels i–k), weaken on 14 June and disappear by 15 June. This time evolution is qualitatively consistent with the mountain wave forecasts in Figure 3 of *Höpfner et al.* [2006b].

[11] Similar maps of brightness temperature perturbations T'_B from channel 72, which peaks ~6 km higher near 30 hPa, revealed clear oscillations (not shown) that are ~180° out of phase with those in Figure 2, indicating a vertical wavelength $\lambda_z \approx 12$ km. A stationary hydrostatic mountain wave has a theoretical vertical wavelength $\lambda_z = 2\pi U/N$, where U is horizontal wind speed orthogonal to wave phase fronts and N is buoyancy frequency. On 12–13 June, Met Office analyses over the AP at 30–80 hPa yield $U \approx 35$ m s^{-1} and $N \approx 0.018$ rad s^{-1}, and thus $\lambda_z \approx 12$ km, consistent with the observational estimate. Thus the

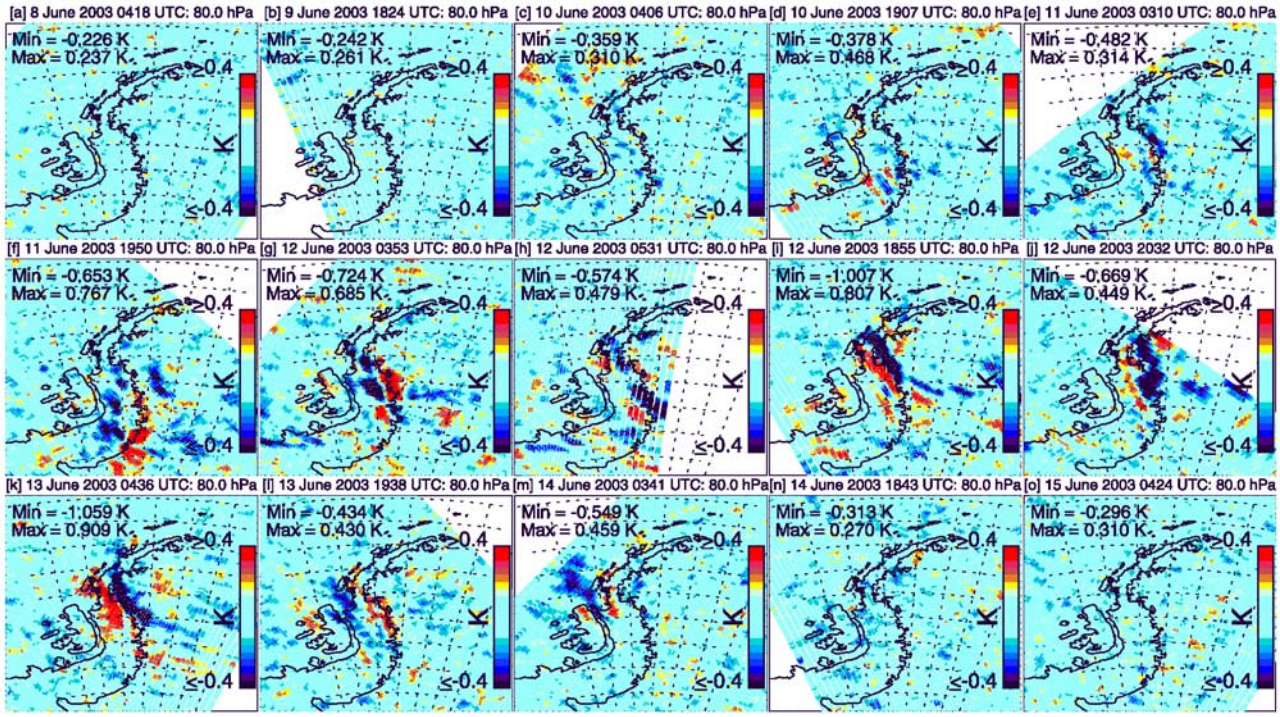

Figure 2. Brightness temperature perturbations T'_B, extracted from 80 hPa AIRS radiances (see text for details), for select overpasses of the AP, in chronological order from (a) top-left, 8 June 0418 UTC, to (o) bottom-right, 15 June 0424 UTC. Date and time of each overpass is given in plot title, as well as maximum and minimum T'_B values.

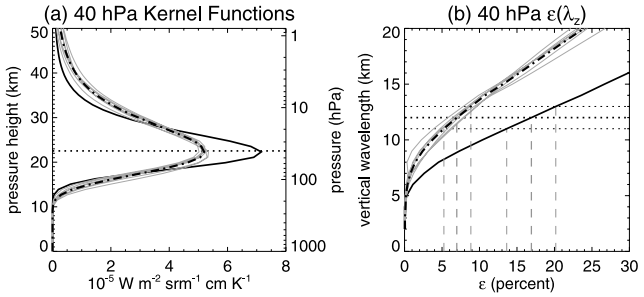

Figure 3. (a) Gray curves show vertical weighting functions for AIRS channels 64, 88, 90, 94, 100, 106 and 118, spanning wavenumbers 665.015–678.839 cm^{-1}, and the corresponding mean (black broken curve). Solid curve shows weighting function for channel 71 (666.773 cm^{-1}). (b) Corresponding attenuations ϵ as a function of λ_z.

observed oscillations are consistent with stationary AP mountain waves.

4. Wave Temperature Amplitudes at PSC Height

[12] To assess the impact of these mountain waves on NAT formation, we must infer peak wave temperature amplitudes $\hat{T}$ at the ~21 km geometric height (~40 hPa) of the NAT PSCs in Figure 1.

[13] Gray curves in Figure 3a plot vertical nadir weighting functions of a collection of AIRS 15 μm channels that peak near 40 hPa with similar properties. We average radiances from these channels, as for the 80 hPa radiances in Figure 2, into a mean radiance scene with reduced noise. As a cross check, we separately analyze radiances from channel 71 that peaks more sharply at 40 hPa. These weighting functions were computed using the radiative transfer model of L. Hoffmann and M. J. Alexander (Retrieval of stratospheric temperatures from AIRS radiance measurements for gravity wave studies, submitted to *Journal of Geophysical Research*, 2008) using a high-latitude winter temperature profile.

[14] These broad weighting functions attenuate the amplitude of any gravity wave in the scene as

$$\frac{\hat{T}_B}{\bar{T}_B} = \epsilon(\lambda_z)\frac{\hat{T}}{\bar{T}}, \qquad (1)$$

where $\hat{T}_B$ is (measured) peak brightness temperature amplitude, ϵ is the attenuation and overbars denote background values. Figure 3b plots $\epsilon(\lambda_z)$ for these 40 hPa channels by scaling the relative radiance response functions of Hoffmann and Alexander (submitted manuscript, 2008) using equation (5) of *Alexander and Barnet* [2007] and $\bar{T} \approx \bar{T}_B \approx 195$ K. For $\lambda_z \sim 12$ km, $\hat{T}_B$ is ~7% of the actual wave temperature amplitude $\hat{T}$ for the multichannel 40 hPa radiances, and ~17% for channel 71 radiances.

[15] Figure 4 plots 40 hPa T' perturbations, derived by scaling T'_B fields by ϵ^{-1} values at λ_z = 12 km, for overpasses on 12 and 13 June. Left panels used multichannel 40 hPa radiances, right panels used channel 71 radiances. Despite very different T'_B and ϵ values, each returns the same independent estimates of $\hat{T} \approx 12$ K on 12 June and ≈10 K on 13 June. For an error of ±1 km in λ_z, the corresponding uncertainty in ϵ (see Figure 3b) leads to error bars of ~±2–4 K in $\hat{T}$.

[16] These mean 40 hPa $\hat{T}$ estimates are probably lower bounds. The finite horizontal width of individual AIRS measurements reduces wave amplitude. More importantly, our 3 × 3 point smoothing, while reducing small-scale noise, also reduces $\hat{T}_B$ values. Comparisons of smoothed and unsmoothed scenes (not shown) suggest reductions of ~20–30%. Thus actual values could be nearer 15 K.

5. Discussion and Summary

[17] Our inferred 40 hPa amplitudes of 10–15 K for the AP mountain waves measured by AIRS validate the $\hat{T}$ = 10–15 K values used by *Höpfner et al.* [2006b], based on hindcasts with the Mountain Wave Forecast Model [*Eckermann et al.*, 2006a]. When inserted into their microphysical model, *Höpfner et al.* [2006b] showed that AP waves of this amplitude formed ice. Solid NAT particles nucleated on this ice and survived downstream. Only this nucleation scenario reproduced the observations in Figure 1. Thus these AIRS observations validate the *Höpfner et al.* [2006b] mountain wave explanation of this observed NAT outbreak.

[18] This event represents a remarkable observational verification of the viability of the "mother cloud" [*Fueglistaler et al.*, 2002] or "salt shaker" [*Dhaniyala et al.*, 2002] theory of vortex-wide solid NAT formation and growth driven by ice formed in isolated pockets of stratospheric mountain wave activity. The AP mountain waves observed here have horizontal wavelengths $\lambda_h \approx 300$ km. The cold phases where ice forms are perhaps no more than 30 × 100 km^2 in horizontal extent. Yet, in this case, these small regions of mountain wave-induced ice production prove sufficient to convert the edge of the Antarctic vortex from totally NAT free (Figures 1a–1c) to being fully populated with NAT PSCs (Figures 1e–1f) over a period of less than a week.

[19] Almost all research on mountain wave-induced NAT has focused on the Arctic, where temperatures are warmer

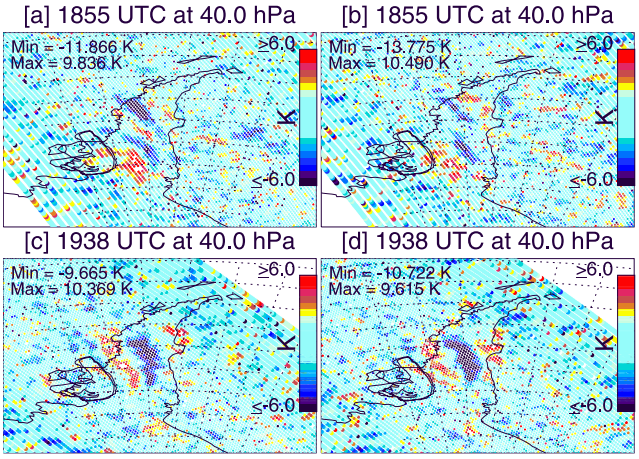

Figure 4. Inferred 40 hPa T' perturbations at 1855 UTC on 12 June (top row) and 1938 UTC on 13 June (bottom row), derived by scaling T'_B fields by $\epsilon^{-1}(\lambda_z)$ for λ_z = 12 km. Left panels used multichannel 40 hPa radiances, right panels used channel 71 radiances.

and mountain wave effects are relatively more important than in the Antarctic [e.g., *Carslaw et al.*, 1998]. Nonetheless, the earliest observations of Antarctic PSCs and ozone loss often showed both forming first over the AP and spreading out from there [*Cariolle et al.*, 1989; *Ricaud et al.*, 1995]. Subsequent observations show PSCs clustering near the AP, yet *Wang et al.* [2008] have discounted any significant role for AP mountain waves in this, stressing instead synoptic uplift by weather systems. Synoptic-scale dynamics alone cannot explain the NAT outbreak in Figure 1 [*Höpfner et al.*, 2006b], highlighting again the central role of AP mountain waves in initiating this particular NAT outbreak.

[20] AP mountain wave-induced PSCs will also activate chlorine, leading to some early-winter ozone loss during daylight hours [e.g., *Carslaw et al.*, 1998; *Kühl et al.*, 2004]. Their overall role in ozone loss is likely limited, of course, since synoptic PSC decks deep within the vortex process more chlorine and can account for observed springtime ozone losses. However, NAT PSCs are central to the denitrification that accentuates this ozone loss, since STS particles do not grow to sufficient sizes to settle out gravitationally to any significant extent [*Tabazadeh et al.*, 2001]. Thus the present work suggests an important role for Antarctic mountain waves in initiating "NAT rock" growth and denitrification at freezing-belt latitudes, along similar lines to that delineated from modeling studies in the Arctic [e.g., *Mann et al.*, 2005].

[21] **Acknowledgments.** SDE, DLW and MJA were supported by NASA's Earth Science Mission Directorate (contract NNH08AE43I).

References

Alexander, M. J., and C. Barnet (2007), Using satellite observations to constrain parameterizations of gravity wave effects for global models, *J. Atmos. Sci.*, *64*, 1652–1665.

Alexander, M. J., and H. Teitelbaum (2007), Observation and analysis of a large amplitude mountain wave event over the Antarctic peninsula, *J. Geophys. Res.*, *112*, D21103, doi:10.1029/2006JD008368.

Cariolle, D., S. Muller, F. Cayla, and M. P. McCormick (1989), Mountain waves, polar stratospheric clouds, and the ozone depletion over Antarctica, *J. Geophys. Res.*, *94*, 11,233–11,240.

Carslaw, K. S., et al. (1998), Increased stratospheric ozone depletion due to mountain-induced atmospheric waves, *Nature*, *391*, 675–678.

Dhaniyala, S., K. A. Mckinney, and P. O. Wennberg (2002), Lee-wave clouds and denitrification of the polar stratosphere, *Geophys. Res. Lett.*, *29*(9), 1322, doi:10.1029/2001GL013900.

Eckermann, S. D., A. Dörnbrack, S. B. Vosper, H. Flentje, M. J. Mahoney, T. P. Bui, and K. S. Carslaw (2006a), Mountain wave-induced polar stratospheric cloud forecasts for aircraft science flights during SOLVE/THESEO 2000, *Weather Forecast.*, *21*, 42–68.

Eckermann, S. D., et al. (2006b), Imaging gravity waves in lower stratospheric AMSU-A radiances, Part 2: Validation case study, *Atmos. Chem. Phys.*, *6*, 3343–3362.

Eckermann, S. D., J. Ma, D. L. Wu, and D. Broutman (2007), A three-dimensional mountain wave imaged in satellite radiance throughout the stratosphere: Evidence of the effects of directional wind shear, *Q. J. R. Meteorol. Soc.*, *133*, 1959–1975.

Fueglistaler, S., B. P. Luo, C. Voigt, K. S. Carslaw, and T. Peter (2002), NAT-rock formation by mother clouds: A microphysical model study, *Atmos. Chem. Phys.*, *2*, 93–98.

Höpfner, M., et al. (2006a), Spectroscopic evidence for NAT, STS, and ice in MIPAS infrared limb emission measurements of polar stratospheric clouds, *Atmos. Chem. Phys.*, *6*, 1201–1219.

Höpfner, M., et al. (2006b), MIPAS detects Antarctic stratospheric belt of NAT PSCs caused by mountain waves, *Atmos. Chem. Phys.*, *6*, 1221–1230.

Kühl, S., A. Dörnbrack, W. Wilms-Grabe, B.-M. Sinnhuber, U. Platt, and T. Wagner (2004), Observational evidence of rapid chlorine activation by mountain waves above northern Scandinavia, *J. Geophys. Res.*, *109*, D22309, doi:10.1029/2004JD004797.

Lowe, D., and A. R. MacKenzie (2008), Polar stratospheric cloud microphysics and chemistry, *J. Atmos. Sol. Terr. Phys.*, *70*, 13–40.

Mann, G. W., K. S. Carslaw, M. P. Chipperfield, S. Davies, and S. D. Eckermann (2005), Large NAT particles and denitrification caused by mountain waves in the Arctic stratosphere, *J. Geophys. Res.*, *110*, D08202, doi:10.1029/2004JD005271.

Ricaud, P. D., et al. (1995), Polar stratospheric clouds as deduced from MLS and CLAES measurements, *Geophys. Res. Lett.*, *22*, 2033–2036.

Tabazadeh, A., E. J. Jensen, O. B. Toon, K. Drdla, and M. R. Schoeberl (2001), Role of the stratospheric polar freezing belt in denitrification, *Science*, *291*, 2591–2594.

Wang, Z., G. Stephens, T. Deshler, C. Trepte, T. Parish, D. Vane, D. Winker, D. Liu, and L. Adhikari (2008), Association of Antarctic polar stratospheric cloud formation on tropospheric cloud systems, *Geophys. Res. Lett.*, *35*, L13806, doi:10.1029/2008GL034209.

M. J. Alexander, Northwest Research Associates, 3380 Mitchell Lane, Boulder, CO 80301, USA.

S. D. Eckermann, Space Science Division, Naval Research Laboratory, Code 7646, Washington, DC 20375, USA. (stephen.eckermann@nrl.navy.mil)

L. Hoffmann, Forschungszentrum Jülich, Leo-Brandt-Str., D-52425 Jülich, Germany.

M. Höpfner, Forschungszentrum Karlsruhe, Postfach 3640, D-76021 Karlsruhe, Germany.

D. L. Wu, Jet Propulsion Laboratory, California Institute of Technology, 4800 Oak Grove Drive, Pasadena, CA 91109, USA.